JOURNAL OF CATALYSIS 105, 120–143 (1987)

Electron Microscopy Characterization of Lanthanum–Cobalt Intermetallic Catalysts

Z. L. WANG,* C. COLLIEX,*,[1] V. PAUL-BONCOUR,† A. PERCHERON-GUEGAN,† J. C. ACHARD,† AND J. BARRAULT‡

*Department of Physics, Arizona State University, Tempe, Arizona 85287; †Laboratoire de Chimie Métallurgique des Terres Rares, ER CNRS 209, 1 Place A. Briand, 92190 Meudon-Bellevue, France; and ‡Laboratoire de Catalyse en Chime Organique, UA CNRS 350; 40 avenue du Recteur Pineau, 86022 Poitiers, France

Received November 4, 1986

A comparison of the detailed structural and chemical arrangements of several cobalt/lanthanum or cerium catalytic systems is made by using different high-resolution electron microscopy techniques. Previous synchrotron X-ray absorption measurements have provided a rather accurate description of the environment of cobalt atoms, suggesting the existence of a nonnegligible number of Co–O bonds. Using a combination of X-ray emission spectroscopy (EDX), electron energy loss spectroscopy (EELS), high-resolution lattice imaging (HREM), we show that the intermetallic compounds, after the syngas reaction, display general features very similar to the model supported Co on La_2O_3 system, while the Co on CeO_2 specimen is quite different. In agreement with EXAFS and XANES studies, we found a very similar environment for the Co particles (partially oxidized in surface) in the $LaCo_5$ and Co/La_2O_3 cases. Moreover, in both systems a catalytic carbon deposit sets apart cobalt from lanthanum oxide in contrast with the Co/CeO_2 specimen. The cobalt particles constitute the "active site" in these compounds and it governs their catalytic properties. As a matter of fact the same selectivity is observed in $LaCo_5$ as for Co/La_2O_3, contrarily to Co/CeO_2, which is much less active and produces only CO_2. These different behaviors could be interpreted in terms of different structural affinities between the rare-earth oxide and the catalytic carbon.

INTRODUCTION

Intermetallic $RE–Me_5$ compounds, such as $LaCo_5$, have been used as active and selective catalysts in chemical reactions involving (CO, H_2) mixtures, i.e., syngas conversion (*1*). Though they have been the subject of many investigations with different physical and chemical techniques for several years, the relationship between the recorded catalytic properties and the catalyst structure is not fully understood. However, there exists a general agreement that the observed activation is associated with a partial transformation of the intermetallic compounds into a metal–support system, likely of the type metal–rare earth oxide. It was even possible to mention the activation as a new way of producing oxide-supported catalysts (*2*). The comparison of these catalysts with more common metal–support systems is therefore of particular interest.

Using different methods of bulk and surface characterization, mostly synchrotron radiation absorption measurements, Barrault *et al.* (*3*) have published a set of results which supports the assumption of a partial transformation. They have compared two families of catalysts: intermetallic compounds prepared by induction melting under vacuum and supported catalysts prepared by impregnating various oxide supports with an aqueous solution of cobalt nitrate, both before and after (CO, H_2) reaction. For the lanthanum–cobalt intermetallic product, an electron microscopy analy-

[1] Permanent address: Laboratoire de Physique des Solides, bldg 510, Université Paris-Sud, 91405 Orsay, France.

0021-9517/87 $3.00

sis shows that the used catalyst consists of complex nodules from which carbon filaments emerge, grown from small metallic particles. Similar metal–carbon composites have been obtained from CO catalytic decomposition by various alloys (*4*). The catalytic carbon deposited *in situ* during the chemical reaction therefore plays a significant role, together with the small metallic particles of size ranging roughly from about two to a few tens of nanometers. These particles are mostly composed of cobalt. One can also identify, in the specimen, well-isolated lanthanum oxide platelets.

Near-edge fine structures (XANES) and extended oscillations (EXAFS) on the cobalt X-ray absorption K edge are rather different from those for bulk cobalt. The following features are deduced from an analysis of the synchrotron absorption data:

—An edge shift toward higher energies relative to the Co metal edge, but of smaller value than for a reference Co_3O_4 edge.

—The near edge shape is also intermediate between those recorded for Co and Co_3O_4 specimens. It is qualitatively similar to XANES profiles recorded *in situ* and in real time during the reduction of Co_3O_4 particles (*5*, *6*).

—The EXAFS oscillations have been processed following a well-established procedure (*7*). They show that distances from Co to the first four shells agree with interatomic distances in metallic Co. On the other hand, the values of the average coordination numbers deviate noticeably: the number of neighbors, scaled to that for bulk Co, is smaller than unity and decreases with the shell radius. This suggests that only a fraction of the cobalt atoms is involved in metallic bonding. Moreover the authors mention a weak prepeak in the range 1.5–1.6 Å which could be attributed to the presence of Co–O or Co–C close neighbors pairs.

All these characterization methods are macroscopic: they deal with specimen volumes on the millimeter scale rather than on the nanometer scale. The above information is thus an average over a very large number of Co atoms, which are not all involved in the same type of component.

As the specimen is highly inhomogeneous (as indicated from the first electron microscopic (EM) observations), it is necessary to investigate the structural and chemical properties of these catalysts with more local probes. A selected-area diffraction and dark-field imaging study of cobalt microparticles has been reported by Audier and Guyot (*8*) in which case the particles were obtained from carbon monoxide disproportionation. In following papers, these authors investigated the crystallographical and morphological properties of such cobalt particles with carbon in insertion (*9*).

The purpose of the present paper is to use modern analytical and high-resolution electron microscopes to study on a very small scale the structure and chemistry of used intermetallic $LaCo_5$ catalysts and to compare the results with those obtained for more conventional metal systems supported on rare earth oxides. A preliminary account has been published in (*10*).

MATERIALS AND METHODS

Four families of specimens have been studied, two $LaCo_5$ ones and two supported ones. They shall be referred to as $LaCo_5$ (a) and (d), Co/La_2O_3, and Co/CeO_2. The intermetallic ones correspond to the initial alloy (a) and to a pretreated specimen (d) which had been oxidized for 3 h at 350°C and reduced for 2 h at 400°C before the catalytic reaction. The comparison is made with two samples of metallic Co supported on rare earth oxides, La_2O_3 in one case and CeO_2 in the other one.

The catalytic reaction consists of the hydrogenation of carbon monoxide into methane and hydrocarbon compounds:

$$(CO, H_2) \rightarrow (CH_4; C_nH_{2n}; C_nH_{2n+2}).$$

This reaction requires both CO and H_2 dis-

TABLE 1

Summary of the Catalytic Properties of $LaCo_5$ Intermetallic and Supported Cobalt Catalysts in the (CO, H_2) Reaction

Catalyst	Pretreatment	Time in hours	Activity $\times 10^3$ (mol h^{-1} g_{Co}^{-1})	Selectivity		
				CH_4	C_2^+	CO_2
$LaCo_5$ (a)	Without	40	7.2	43	11	46
$LaCo_5$ (d)	Oxidized for 3 h at 350°C reduced for 2 h at 400°C	45	20	44	10	46
Co/La_2O_3	Oxidized for 3 h at 350°C reduced for 10 h at 400°C	10	17	45	16	36
Co/CeO_2	Oxidized for 3 h at 350°C reduced for 10 h at 400°C	5	1.0	<5	7	90

sociation at the surface of the catalysts. Secondary products such as H_2O and CO_2 are also generated during the reaction. A few major results are summarized in Table 1, which is an excerpt of an equivalent table in (*3*). It shows that the catalysts offer various levels of activity and different distributions in selectivity for the final products of the (CO, H_2) reaction. The Co/CeO_2 exhibits a behavior rather distinct from the other ones, while the intermetallic compounds have trends similar to Co/La_2O_3. Moreover the pretreatment noticeably shortens the activation period with respect to the initial specimen. Our purpose is to investigate how these different catalytic behaviors may correspond to different structural and chemical properties of the used specimens.

For EM observation, the specimens are ultrasonically dispersed within acetone and deposited on a holey carbon film supported by a conventional copper grid. Most images, diffraction patterns, and analytical measurements have been made on specimen areas protruding over holes in the carbon film (see Fig. 1) to avoid confusion between the catalyst specimen and the underlying film.

The electron microscopes available at the HREM Facility of the Center for Solid State Science at ASU have been used. No single instrument offers top performance for all types of observation or measurement. Consequently, different studies have been made on the different microscopes listed below:

—JEOL 100B (primary voltage 100 kV and $\simeq 10^{-6}$ Torr at the specimen), for the general morphology study by images and selected-area diffraction;

—Philips 400T (primary voltage 120 kV, LaB_6 gun, and $\simeq 10^{-7}$ Torr at the specimen), for X-ray microanalysis (EDX) and EELS on relatively large areas ($\simeq$50 to 100 nm);

—Vacuum Generators HB5 (primary voltage 100 kV, dedicated scanning transmission electron microscope (STEM) field emission gun (FEG), and $<10^{-8}$ Torr at the specimen), for very-high-spatial resolution in microdiffraction and EELS (probe size down to 0.5 nm);

—JEOL 200 CX and 4000 EX (respectively, operated at 200 and 300–400 kV, both using LaB_6 guns, and with a typical vacuum of $\simeq 3 - 5 \times 10^{-6}$ and $3 - 5 \times 10^{-7}$ Torr around the specimen). Both instruments provide structure images. Lattice fringe periodicities are analyzed and measured by optical diffraction. Point resolution is respectively 0.24 and 0.17 nm which makes structure imaging of compounds with lattice distances greater than $\simeq$0.18 nm accessible. Both instruments are equipped with a YAG screen and a TV out-

put connected to a videotape, so that it is possible to record dynamic beam-induced changes of the specimen.

GENERAL CONFIGURATION AND CHEMISTRY OF THE SPECIMEN

Typical micrographs of used catalyst products are shown in Fig. 1. The $LaCo_5$ (a) case (Fig. 1A) consists of rather thick, complex agglomerates from the surface of which emerge carbon fibers with small metallic particles at the extremity. It is not common to find lanthanum oxide flakes near the free surface; generally they lie within the core of these agglomerates as a kind of skeleton to keep all the components together. A similar general topography is found in specimen Co/La_2O_3 with a clearer separation between the long, thick lanthanum oxide platelets and the remainder of the specimen (Fig. 1C); here again many catalytic carbon fibers, supporting small metallic particles at their extremity, are seen all along the outer surface of the specimen. In $LaCo_5$ (d) (Fig. 1B), we observe the same rather complex mixture of clear La_2O_3 flakes with unidentified products, but it is obvious that there is much less catalytic carbon in the form of protruding easily identifiable fibers. Finally the CeO_2 specimen (Fig. 1D). is clearly different, with compact shapes for the oxide support crystals and little carbon resulting from the catalytic reaction discernible on the surface.

X-ray emission spectroscopy (EDX) analysis is used to control the average chemical composition of material volumes typically of a few tenths of a micrometer, defined either by focusing the probe on various areas (such as labeled A, B, C, and D in Fig. 1A) or by defocusing it to cover the whole aggregate.

The observed major families of lines are due to Co, La, and Cu (this last one is a very frequent system peak due to uncollimated radiation interacting with the specimen support copper grid). In a few cases, it was possible also to detect impurities such as Si, Mg, Al. Considering the height ratio between La–L and Co–K lines, it is obvious that there are substantial composition fluctuations between adjacent areas at this micrometer scale. The major metallic components are rather inhomogeneously distributed.

A more quantitative evaluation of the chemical composition can be made by using the Cliff–Lorimer factor (*11*):

$$\frac{C_{La}}{C_{Co}} = K_{La/Co}\frac{I_{La}}{I_{Co}}$$

where I_{Co} and I_{La} are the intensity of the lines after background subtraction. $K_{La/Co}$ is a constant depending on absolute and instrumental factors. It can be written as

$$K_{A/B} = \frac{\varepsilon_B \kappa_B}{\varepsilon_A \kappa_A}$$

where ε is the relative detection efficiency of the Si–Li detector for the measured line (the ratio $\varepsilon_B/\varepsilon_A$ between the La–L_α line at 6.5 kV and the Co–K_α line at 8.7 kV deviates from unity by less than 2% and is neglected) and $\kappa_A = \sigma_A \bar{\omega}_A a_A$ is the product of ionization cross section (σ_A), fluorescence yield ($\bar{\omega}_A$), and partition function of the α-line (a_A). All these terms can be calculated *ab initio* (see for instance Zaluzec (*12*) from which we have extracted the relevant values for κ_A and κ_B). Typical results of this EDX analysis are summarized in Table 2. It shows different average values of Co/La or Co/Ce ratio, the intermetallic catalysts being much richer in Co than the supported ones (which reflects the macroscopic chemical composition of the initial samples); it also proves unequal inhomogeneity levels at this spatial resolution scale of a fraction of a micrometer. Specimen $LaCo_5$ (a), which could be described as inhomogeneous because of fluctuations of a factor 2 on Co/La ratio, is actually much more homogeneous than the Co/La_2O_3 one which exhibits quite different spectra when one selects adjacent areas of the specimen, some of them with negligible cobalt, while the next ones contain no lanthanum.

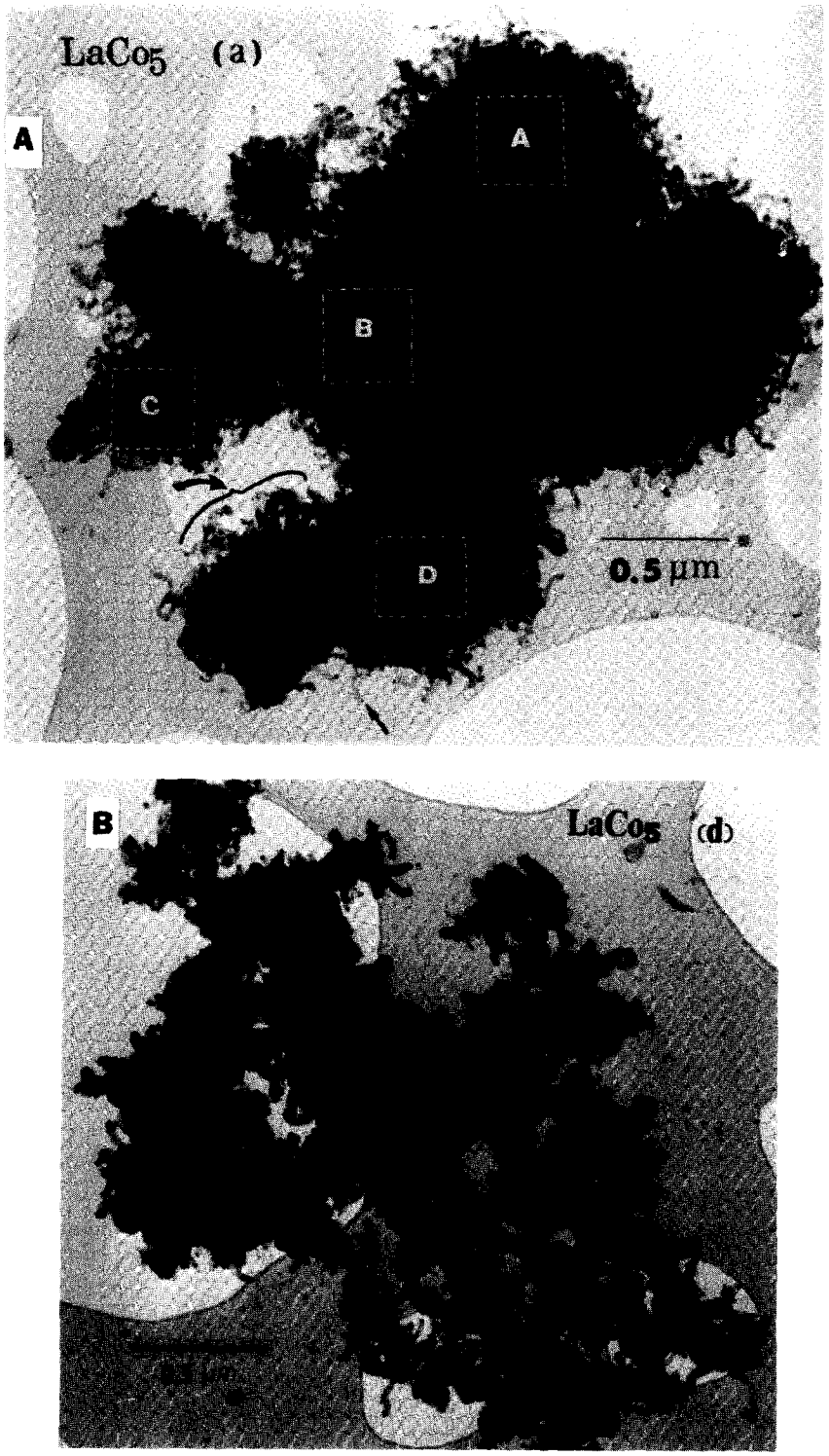

FIG. 1. Typical low-magnification micrographs of the four systems: (A) $LaCo_5$ (a); (B) $LaCo_5$ (d); (C) Co/La_2O_3; (D) Co/CeO_2. Areas in A have been selected for EDX analysis and arrows indicate specific features of interest.

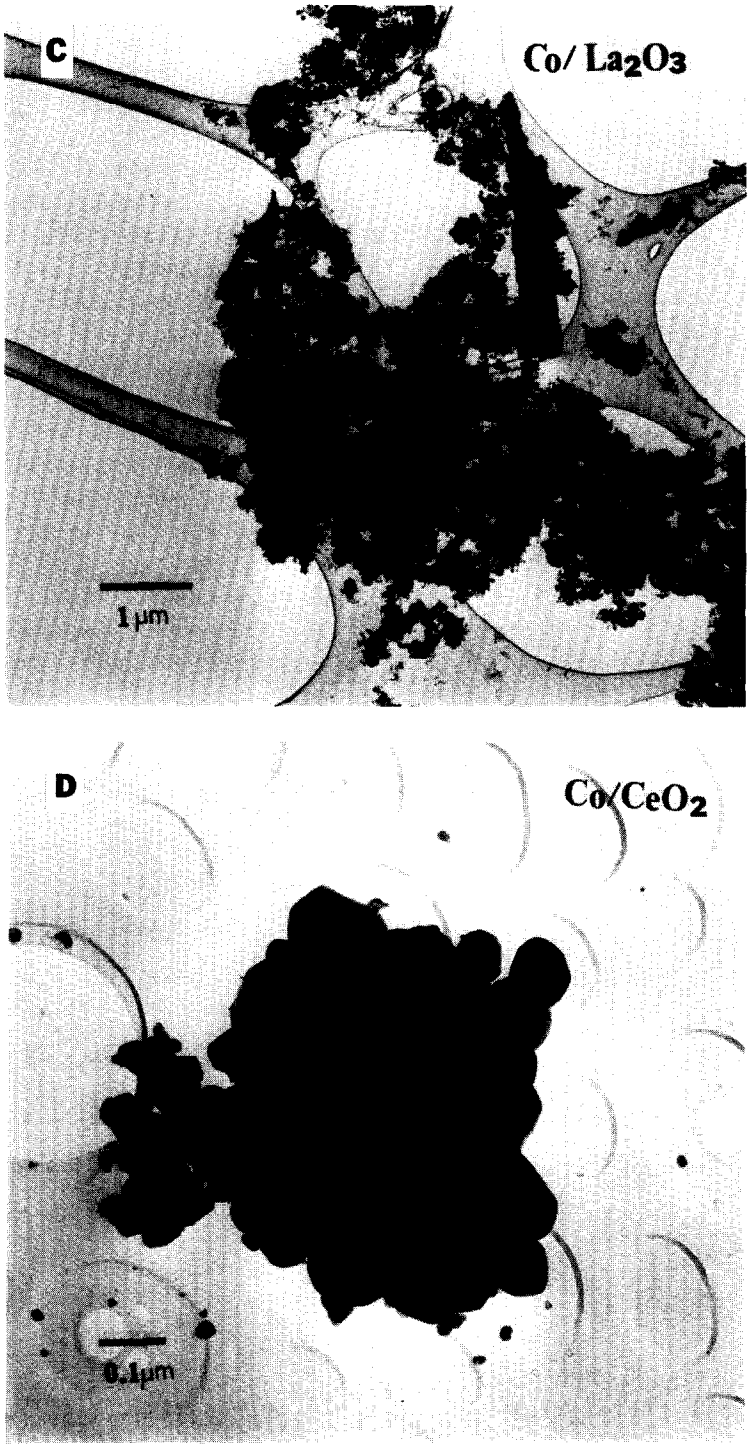

FIG. 1—*Continued.*

TABLE 2

EDX Analysis of the Ratio of the Atomic Concentrations in the Specimens

Catalyst	Average Co/RE	Inhomogeneity[a]
$LaCo_5$ (a)	≃5	3 → 6
$LaCo_5$ (d)	4.4	2 → 8
Co/La_2O_3	≃0.5	0 → ∞
Co/CeO_2	0.4	0.2 → 0.5

[a] The inhomogeneity means the variation range of the atomic concentration ratio Co/RE in the specimens. Results are given in atomic concentration. The used values for K_A and K_B are $K_{Co} = 1.608 \times 10^{-24} \times 58.94$, $K_{La} = 1.034 \times 10^{-24} \times 138.92$. Absorption correction is not included.

ELECTRON ENERGY LOSS ANALYSIS

Electron energy loss spectroscopy (EELS) in the EM is a powerful tool to characterize local electronic and chemical properties. The information is contained in different parts of the EELS spectrum (*13*). In the low energy loss domain, one detects collective valence excitations (plasmons) and significant core excitations from the outer orbitals. These features can be used for a rapid and unambiguous discrimination between the areas with cobalt and those with the rare earth.

Area selection is achieved in the image mode in a conventional transmission electron microscopy (TEM) by placing an aperture below the screen on the small particle of interest and typical analyzed sizes are of the order of 20–40 nm in diameter. The low intensity of the signal and the chromatic aberration of the objective lens prevents from achieving higher spatial resolution with this type of EM spectrometer configuration.

As an example of identification, Fig. 2 shows three spectra covering an energy

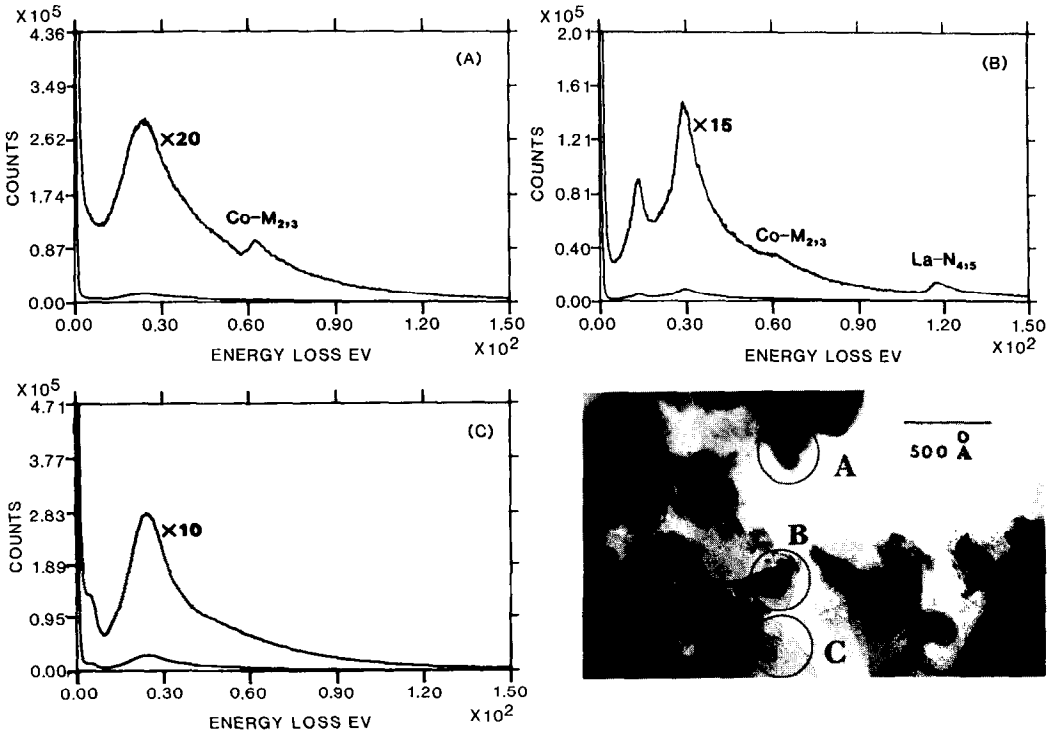

FIG. 2. Low energy loss spectra from well-defined areas, circled in the micrograph, in a $LaCo_5$ (d) specimen. They display the characteristic patterns for (A) metallic cobalt, (B) lanthanum oxide, and (C) carbon.

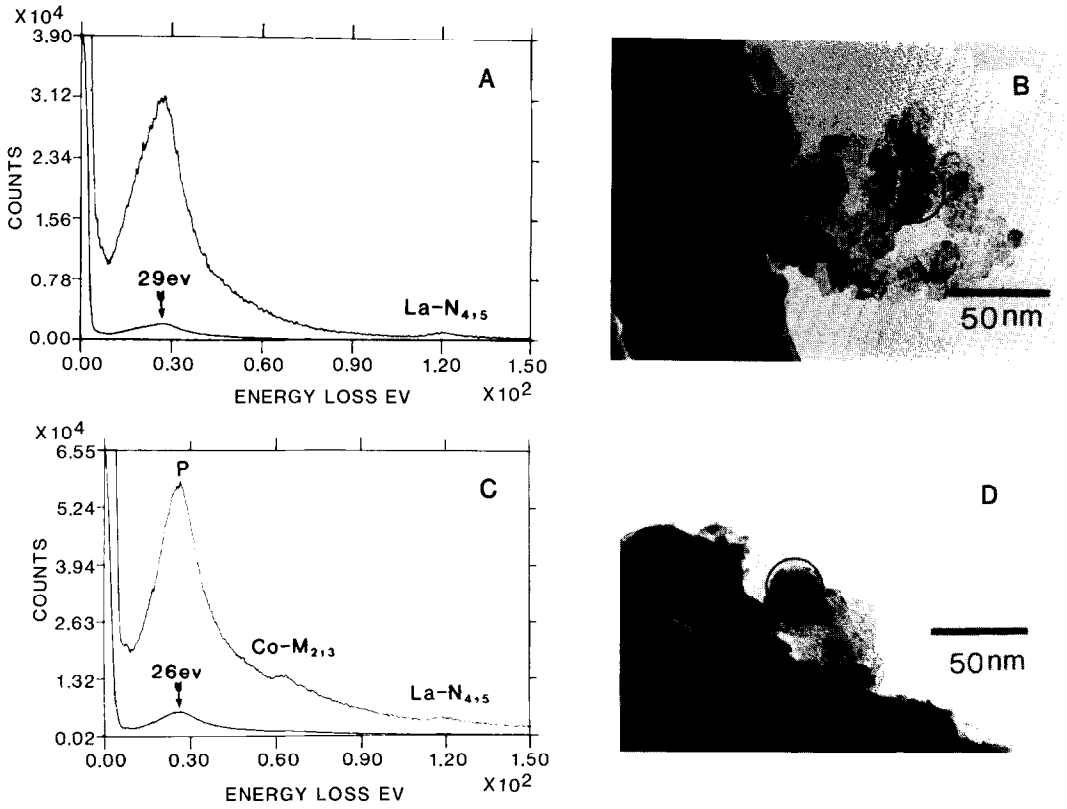

FIG. 3. Unidentified behaviors in the low energy loss spectra of a few compounds (A) corresponds to the area circled in (B), and (C) to the one circled in (D). See text for discussion.

loss range 0–150 eV and recorded from adjacent areas in a $LaCo_5$ (d) specimen. Spectrum 2B can be attributed to a La_2O_3 crystal with a plasmon at ≃14 eV, a lanthanum O_{23} peak at ≃29 eV and a lanthanum N_{45} edge at ≃118 eV. The weaker peak slightly above 60 eV should be due to a small content of Co. Spectrum 2A is on the other hand quite representative of Co metal. It is more similar to the profile published by Wehenkel and Gauthé (*14*) than to the CoO spectrum in the EELS atlas of Ahn and Krivanek (*15*): there is no peak at ≃6 eV and no oscillation between 30 and 60 eV. In all cases the 63-eV edge (Co–M_{23} edge) is a clear test of the presence of cobalt. Spectrum 2C recorded outside metal particles is representative of carbon; the plasmon peak is similar to the cobalt one except for a slight shift of ≃1.5 eV toward higher energy, but the absence of the M_{23} edge at 63 eV is a much more convenient way of avoiding confusion between carbon and cobalt.

In some cases, the interpretation of the spectra is not clear and two examples are gathered in Fig. 3. Figure 3A is the spectrum from the small particle shown in Fig. 3B, with a characteristic La–N_{45} peak, but with a low energy loss spectrum from 10 to 30 eV quite different from the normal one (Fig. 2B). Does it correspond to another lanthanum compound, such as a lanthanum carbide oxide? Such interpretations cannot be ruled out. Another unexplained feature at this level of spatial resolution is the occurrence of spectra such as shown in Fig. 3C. It has a single plasmon loss peak slightly shifted with respect to the cobalt peak and two clear edges of cobalt and lan-

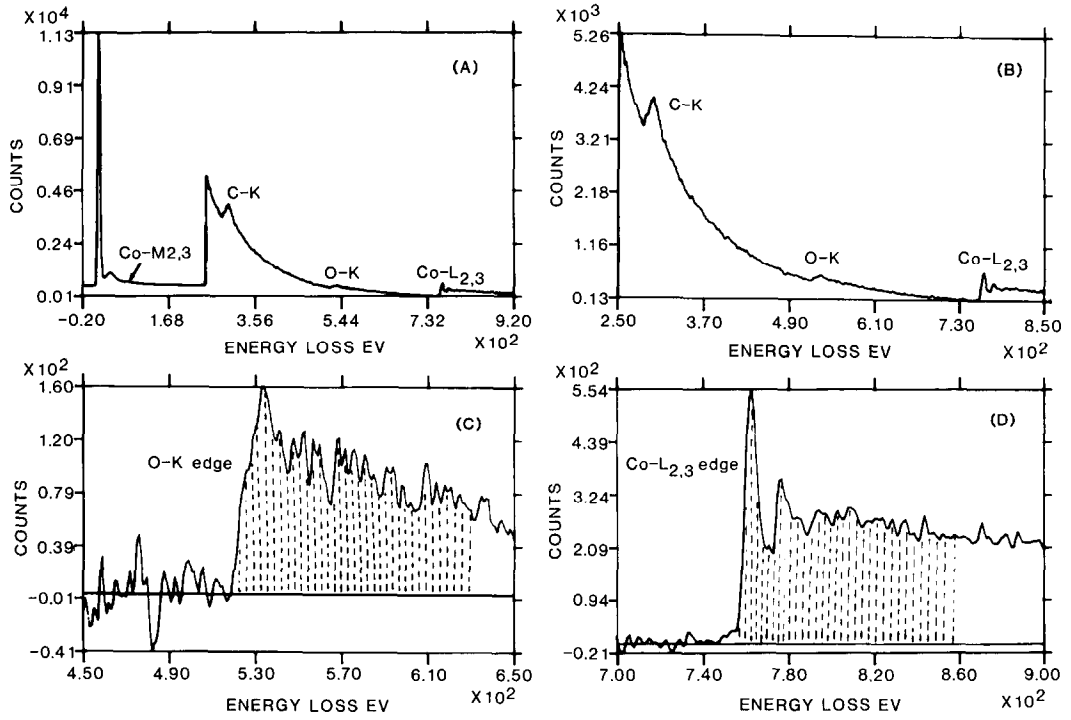

FIG. 4. (A) Core loss edges on a particle of ≈8 nm size. (B) shows the three characteristic signals for C, O, and Co. (C) and (D) show the edges after background subtraction for a semiquantitative analysis.

thanum in the higher energy loss range (the area selected for such a spectrum is shown in Fig. 3D) and it is not obvious at this stage whether this can be interpreted in terms of juxtaposition of lanthanum- and cobalt-rich areas within the analyzed volume, or whether it implies the existence of a cobalt–lanthanum compound.

Generally speaking, EELS has been routinely used to discriminate cobalt-rich from RE-rich particles and to determine on a typical 20-nm scale the relative spatial arrangement of the various components. For instance in $LaCo_5$ (a), it has not been possible to detect adjacent cobalt particles and La_2O_3 platelets, contrary to the (d) specimen. The presence of catalytic carbon is much more important in the first case.

In the VG STEM, a nanometer probe is focused on the specimen; it is possible to select, either in image or microdiffraction mode, single "metallic" particles with diameter as low as a few nanometers and to record the associated EELS spectrum in the energy range ≈300 to ≈800 eV (see Fig. 4). The main components are the carbon K-edge, the oxygen K-edge, and the cobalt L_{23}-edge visible over the noncharacteristic continuously decreasing background (Fig. 4B). The carbon is detected because the cobalt particle is buried within the extremity of a carbon fiber, so that it is generally covered on both surfaces with a variable thickness of catalytic carbon. More interesting is the presence of an oxygen signal in a number of situations: it depends on the metal cluster size and on the existence of free surfaces devoid of carbon coverage. The ratio of oxygen with respect to cobalt can be estimated in a semiquantitative way by using the standard method due to Egerton (*16*):

$$\frac{C_{Co}}{C_O} = \frac{I_{Co}}{I_O} \times \frac{\sigma_O}{\sigma_{Co}},$$

where I_{Co} and I_O are defined after back-

ground subtraction and integrated over a typical 100-eV energy window (see Figs. 4C, 4D) and σ_O and σ_{Co} are the relevant K and L_{23} ionization cross sections as they can be calculated for instance from Sigmak or Sigmal routines (*17*). In the case of Fig. 4 (referring to a ≈8-nm Co particle), one estimates a composition as $CoO_{0.4\pm0.1}$. This number does not have any absolute significance; it only means that in this selected particle, about one-half of the cobalt atoms are involved in Co–O bonds. This result, obtained from a volume of specimen of about 10^5 cobalt atoms, is rather consistent with the X-ray EXAFS data for a volume of $\simeq 10^{18}$ cobalt atoms.

HIGH-RESOLUTION ELECTRON MICROSCOPY

EELS indicates that the final product, after catalytic reaction, is a complex combination of RE, cobalt, carbon, and oxygen. For a more complete identification, high-resolution electron microscopy (HREM) imaging of lattice planes in small (1- to 20-nm) particles has been systematically performed. An optical diffraction (OD) analysis of the micrographs was used to measure interreticular distances and angles with sufficient accuracy. For identification Table 3 shows useful crystallographic data on known phases. A similar method has already been applied to various test or real catalysts. For instance, the work of Smith *et al.* on "graphimets" (*18*) is technically very similar to the present study; they show that the intercalated metal element (Fe, Co, Ni, Cu, Pt) is present as small islands of metal or of metal oxide on the surface of graphite flakes.

The capabilities of HREM microscopy in the case of complex systems, like those under investigation, are very impressive as illustrated below for the different type of specimens.

1. Specimen $LaCo_5$ (a)

HREM images mostly show cobalt particles embedded within carbon fibers; the La_2O_3 platelets do not appear along the edges of the specimen. Metallic particles are generally made of cobalt-α hexagonal as shown in Fig. 5, in which one does not detect any contamination except the catalytic carbon coverage. An interesting observation is the existence of faulted Co particles. Co metal has two structures, either hcp or fcc, and the stacking sequence of the hexagonal close-packed planes does not follow either the two-plane ABAB periodicity of the hcp structure or the three-plane

TABLE 3

Crystal Lattice Data Used for Structure Identification (All Distances Are Given in Angströms)[a]

Type of material	Index of planes	Plane distance	Type of material	Index of planes	Plane distance
Co-α	$10\bar{1}0$	2.17	Co-β	111	2.05
hcp	0002	2.04	fcc	200	1.77
	$01\bar{1}1$	1.92	$a = 3.55$	220	1.25
$a = 2.51$					
$c = 4.08$					
CoO	111	2.47	Co_3O_4	111	4.67
NaCl type	200	2.13	Spinel H1	200	4.04
fcc	220	1.51	fcc	220	2.86
$a = 4.26$			$a = 8.10$	311	2.44
				222	2.33
				400	2.02
Co_3C	011	4.01	Co_2C	011	4.05
	101	3.70		101	3.75
Orthorhombic	002	3.36	(Fe_2C type)	110	3.38
$a = 4.44$	110	3.32	Orthorhombic	002	3.38
$b = 4.99$	111	2.97	$a = 4.53$	111	3.02
$c = 6.71$	020	2.49	$b = 5.09$	020	2.54
	112	2.36	$c = 6.74$	112	2.39
	200	2.22		200	2.26
	121	2.07		121	2.14
	022	2.00		022	2.02
Co_2C	011	3.11	$C_{graphite}$	0002	3.36
	101	2.43		$10\bar{1}0$	2.13
(Co_2N type)	110	2.42	Hex 2H	$10\bar{1}1$	2.03
	002	2.22	$a = 2.46$	$10\bar{1}2$	1.80
Orthorhombic	020	2.18	$c = 6.72$		
$a = 2.90$	111	2.12			
$b = 4.37$					
$c = 4.44$					
A-La_2O_3	$10\bar{1}0$	3.42	C-La_2O_3	211	4.60
Hexagonal	0002	3.06		222	3.25
	$10\bar{1}1$	2.96	Cubic	400	2.82
$a = 3.94$	$10\bar{1}2$	2.27			
$c = 6.13$	$11\bar{2}0$	1.97	$a = 11.25$	420	2.52
				440	1.99
CeO_2	111	3.12			
Cubic	200	2.71			
$a = 5.41$	220	1.91			

[a] Thanks are due to M. Gasgnier for his help in selecting the useful data.

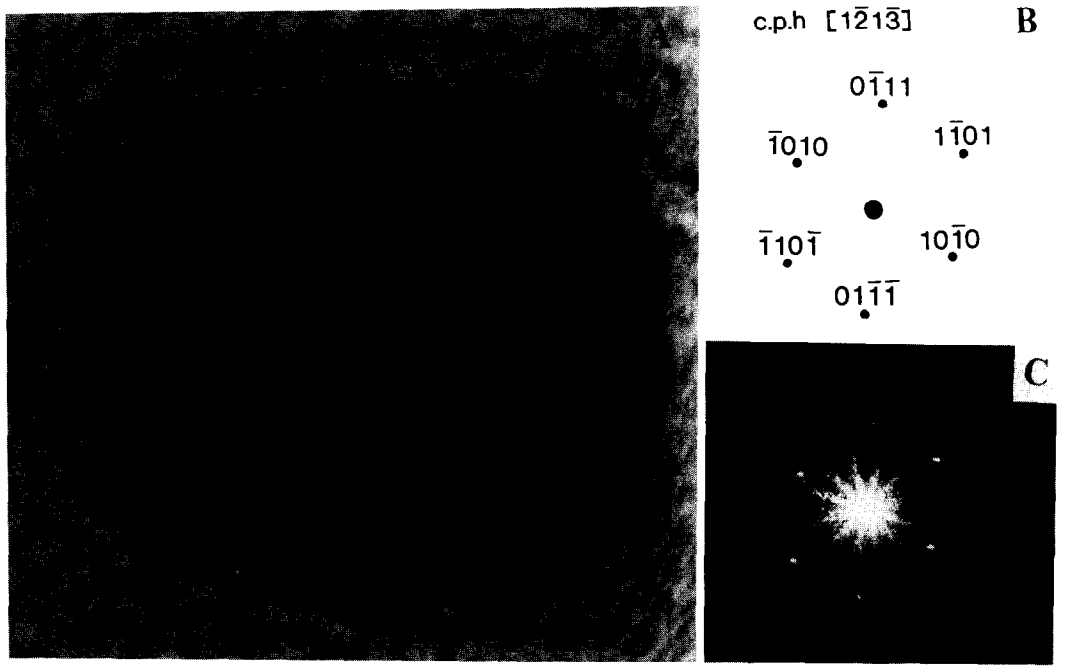

FIG. 5. $LaCo_5$ (a) specimen: (A) Micrograph of a single Co-α particle embedded within catalytic carbon; (B) optical diffraction pattern showing the three directions of the lattice planes; (C) proposed indexation for the OD pattern.

ABCABC periodicity of the fcc one. It may show faults in both sequences or exhibit a random succession of stacking sequences. Diffraction patterns show the superposition of the two types of hcp or fcc contributions; see (*19*) for discussion. In the image the faulting appears as a random succession of parallel fringes perpendicular to the [111] axis. Such a faulted Co particle is visualized under HREM conditions in Fig. 6. One sees the succession of hcp and fcc slabs, with a regular periodicity of two lattice planes ($\simeq$0.42 nm) at the lower part of the particle. The tilted fringes at 0.174 nm are likely due to the $(200)_{fcc}$ planes. On the particle surface, smaller crystals of Co_3O_4 are visible.

Oxygen contamination is a rather general feature which can be observed for particles of any size. Figure 7 concerns a small particle (A) of about 3 nm diameter buried between graphite layers but lying close to the free surface of the specimen. The OD pattern can be indexed as Co-α, with two main sets of planes at 0.217 and 0.205 nm (more intense spots in the OD and lattice distances are shown in the micrograph). Moreover, the OD displays two pairs of extra spots corresponding to $\simeq$0.35 and 0.247 nm, respectively.

A complete analysis on a larger particle is presented in Fig. 8. The major set of lattice fringes extending over the whole particle area and identifiable thanks to a pair of spots (indexed $o(11\bar{1})$ and $o(\bar{1}\bar{1}1)$ in the OD) corresponds to a regular unfaulted pile-up of close-packed planes. In area A, it is the only periodic contribution. But in other areas, B, C, or D, OD analysis reveals other periodicities. The extra spots have been identified as due to a surface layer of CoO (area B), and to a well-defined crystallite of Co_3O_4 near the free surface (area D). Close to the interface between cobalt and catalytic carbon (area C), the (111) spots are elongated: it suggests a dilatation of the spacing between outermost planes, which can be estimated to be of the order of 2–5%.

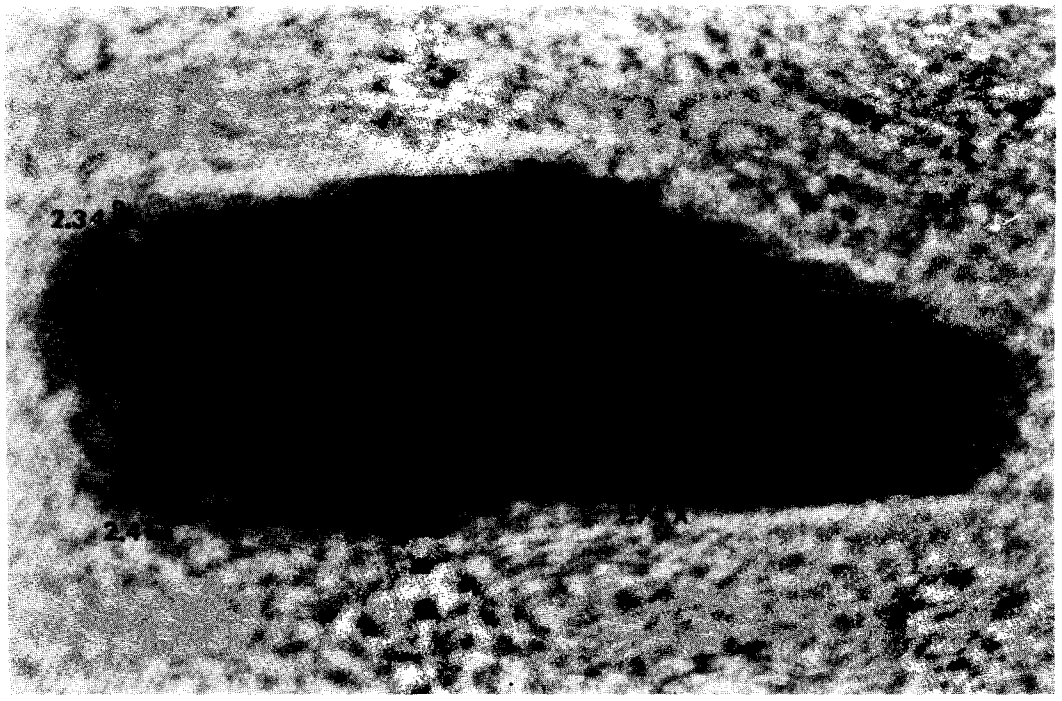

FIG. 6. HREM micrograph of a faulted Co-α particle.

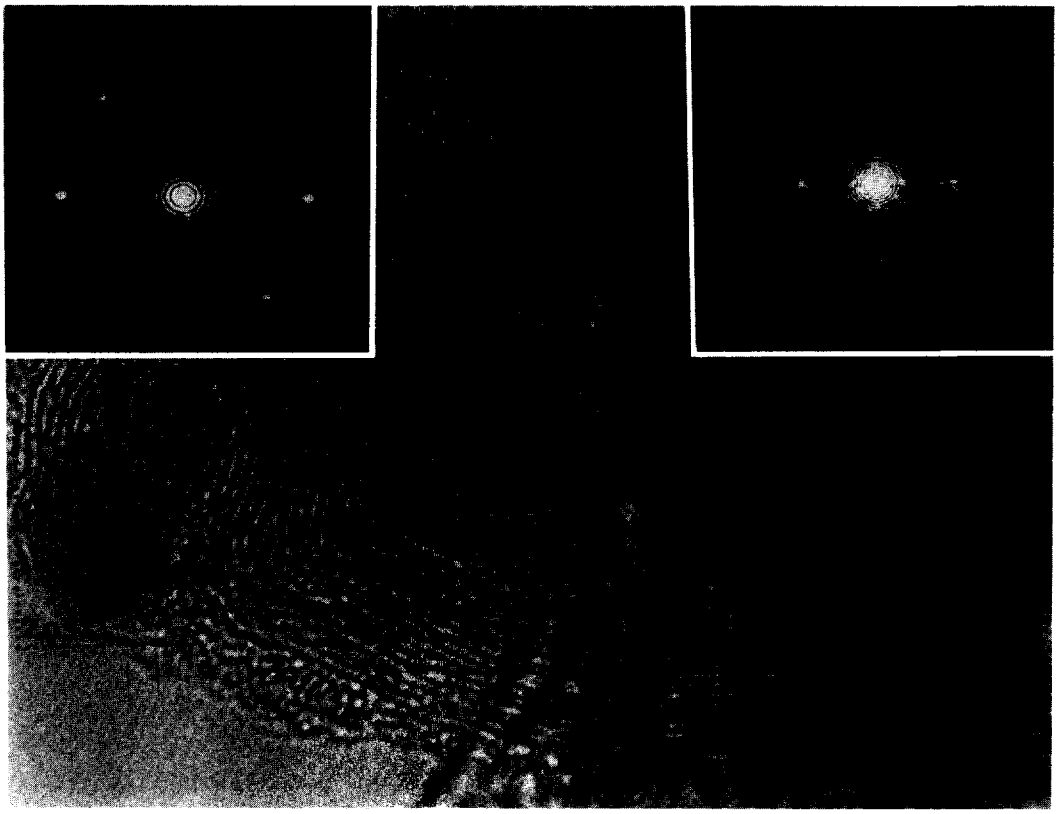

FIG. 7. Micrograph of a small Co-α particle at the edge of a catalytic carbon deposit. Optical diffraction patterns concern the A area on the metallic particle and the B area on the graphite (the spacing is slightly greater than the 0.34-nm (0002) spacing in natural graphite).

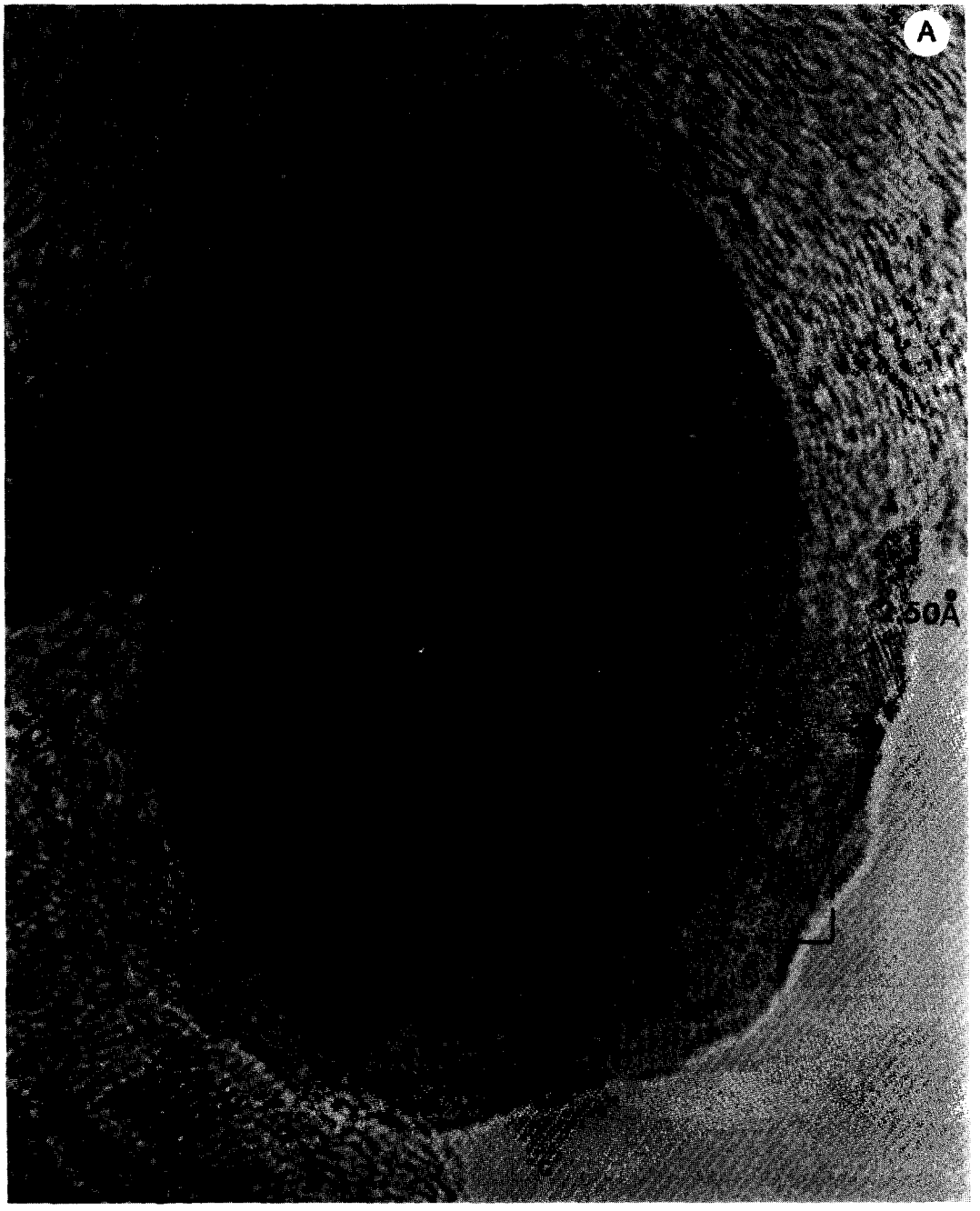

FIG. 8. A. HREM study of a large Co particle in $LaCo_5$ (a) specimen; (A) micrograph showing the localization of reduced areas selected for optical diffraction analysis; (B) a selection of magnified images together with their OD patterns and the proposed solution for indexing.

In this specimen, the Co particles buried within a shell of catalytic carbon are often covered with variable amounts of CoO and Co_3O_4 crystallites which are identified with their lattice arrangements.

2. Specimen $LaCo_5$ (d)

There are a lot of similarities between (d) and (a) specimens. One can identify cobalt particles and find some presence of cata-

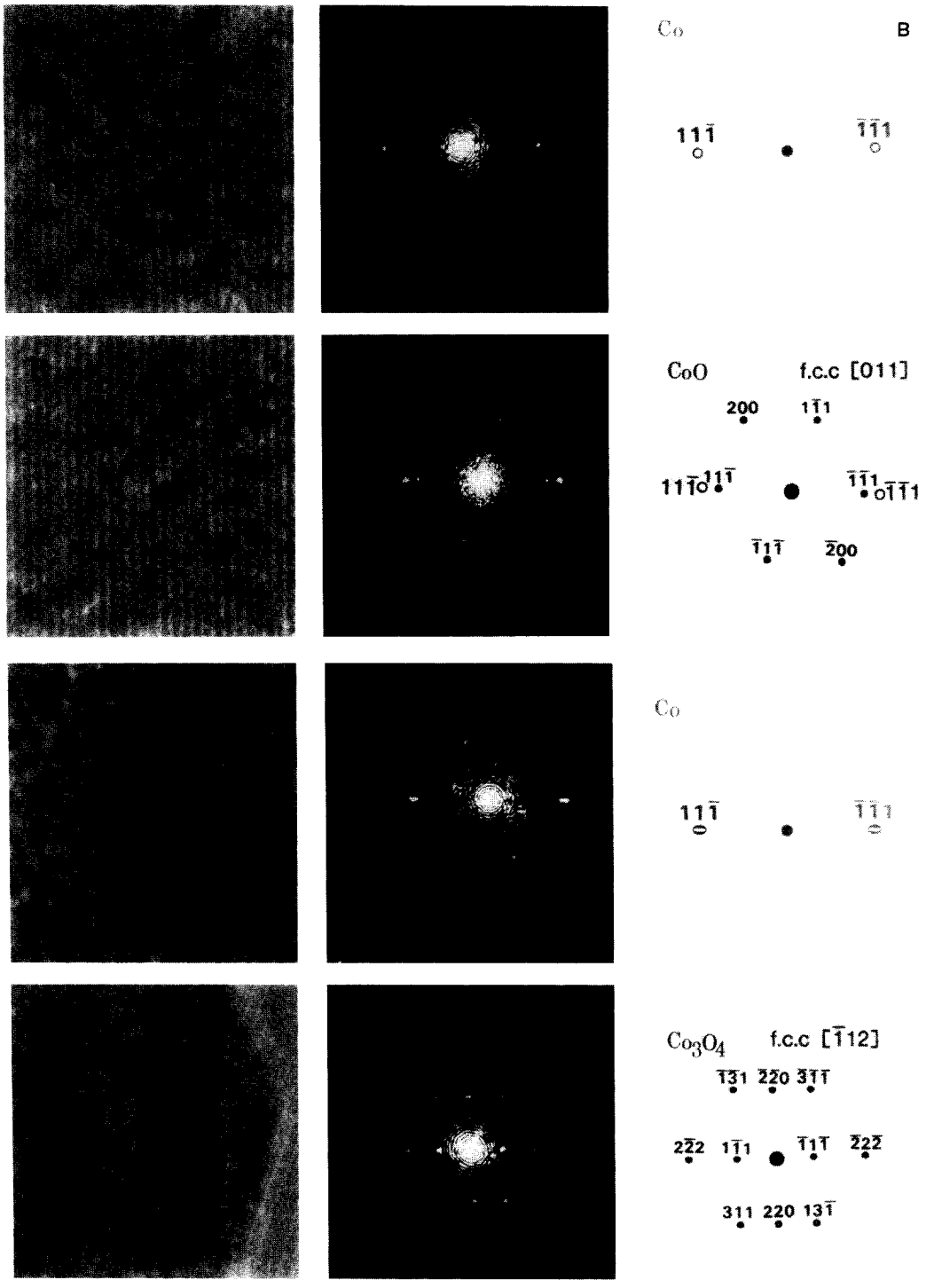

FIG. 8—*Continued.*

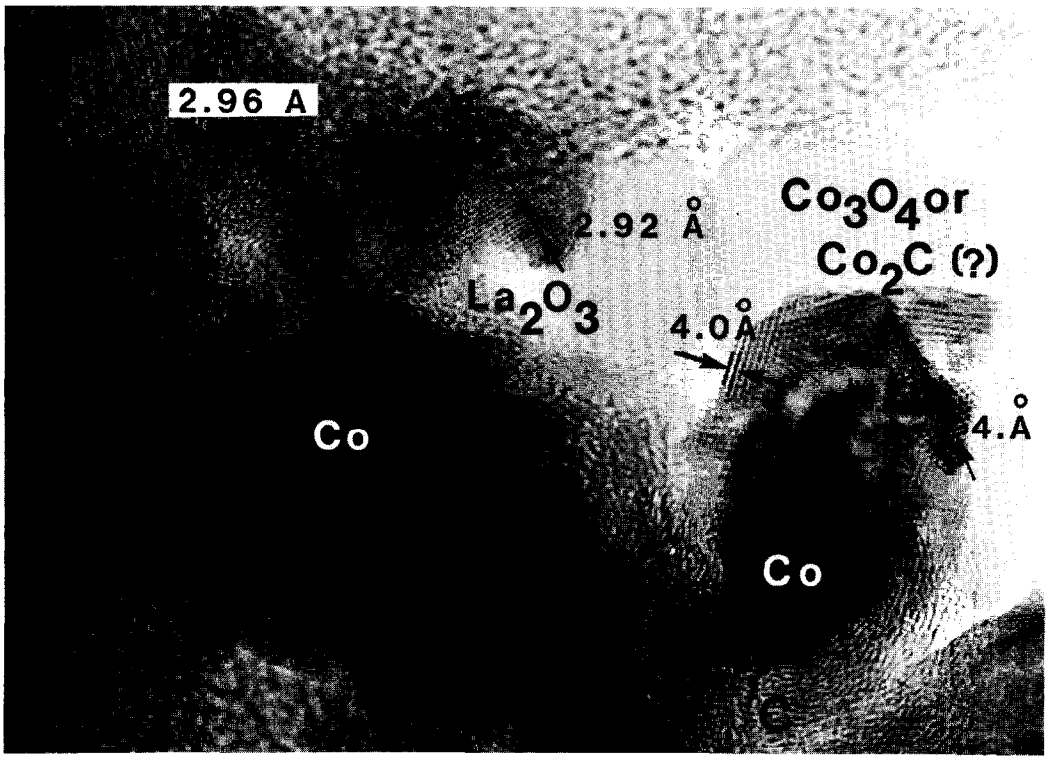

FIG. 9. A HREM micrograph of the typical arrangement of Co particles, catalytic carbon, and rare-earth oxide support in specimen $LaCo_5$ (d).

lytic carbon, but there does not exist as many well recognizable carbon fibers or tubules on the extremity of which the metallic particles are located. On the contrary, one sees a lot of La_2O_3 platelets in the neighborhood, as visible in Fig. 9, which is rather illustrative though it does not show the metallic cobalt lattice planes. Generally the nature and arrangement in this specimen are much more complex than in the previous one, and lattice images involving interreticular distances of 2.55 Å for instance have not been elucidated. It is not too much surprising because many "exotic" phases involving various combinations of lanthanum with oxygen, carbon, H, or CO radicals can likely be found at the end of the chemical reactions (*20*); for instance lanthanum oxide carbide and various cobalt carbide lattice planes could have been identified in certain projections, but one orientation is generally not sufficient for an unambiguous decision with low-symmetry structures.

3. Specimen Co/La_2O_3

Co/La_2O_3 constitutes a well-defined situation in which it is rather straightforward to identify the La_2O_3 platelets, the Co particles, and the catalytic graphite in a number of micrographs. One example is shown in Fig. 10 in which the carbon coverage is an important component of the system, hampering a close contact between the metal particle and the oxide support. The catalytic carbon planes generally seem to wrap the cobalt particles efficiently. In many areas close to the outside surface, smaller crystallites can be detected and generally identified as CoO phases (Fig. 11). It has been possible in this specimen to find again a lot of features already detected in the intermetallic samples, such as the typical faulted cobalt particles (Fig. 12). Different

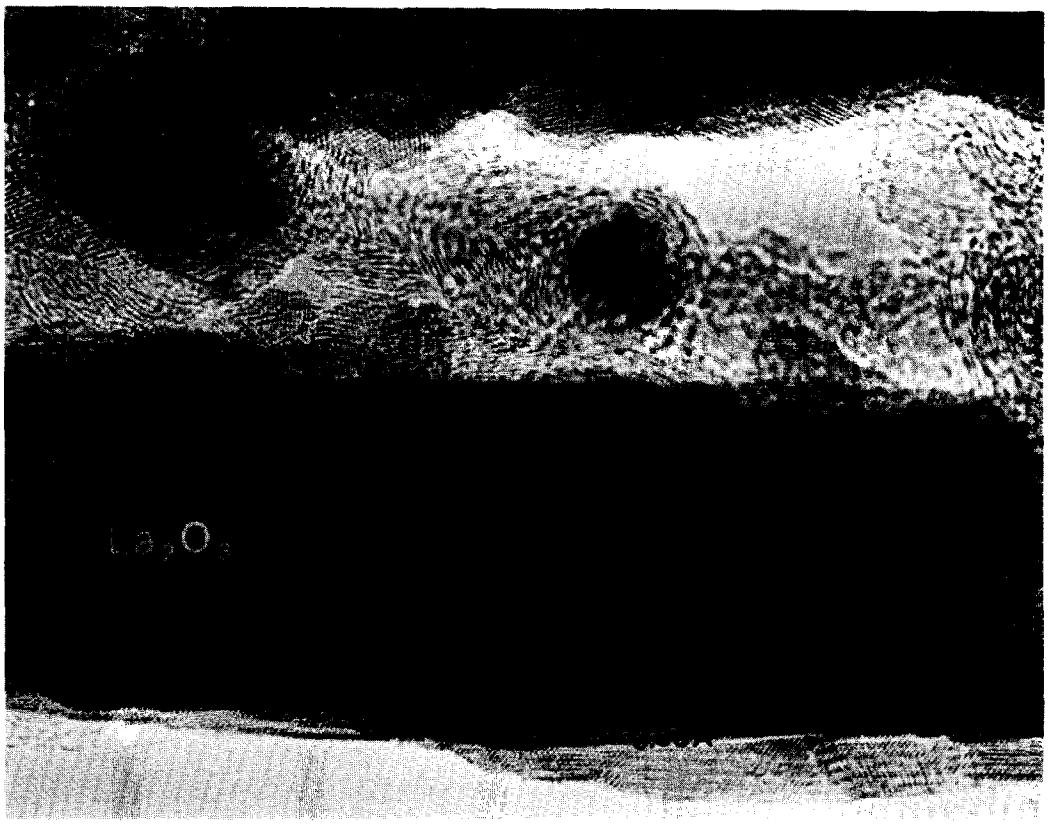

FIG. 10. Specimen Co/La_2O_3 displaying clear Co particles covered with regular shells of catalytic carbon, in the neighborhood of isolated La_2O_3 crystallites.

La_2O_3 phases have been recognized, such as the hexagonal one with lattice plane spacings of 3.5 and 3.05 Å; this latter value being the most commonly seen (it can also be interpreted as due to the (0002) plane of the hexagonal structure). All in all, there are many strong similarities between Co/La_2O_3 and both intermetallic cases, with clearly recognizable products like in (a) and a rather high probability of finding RE oxide platelets close to the free external surfaces of the specimen like in (d).

4. Specimen Co/CeO_2

Co/CeO_2 constitutes a clearly distinct situation from the previous ones. One does not find the characteristic catalytic carbon which is present into variable amounts on all other specimens. The general configuration consists of a CeO_2 isolated crystal recognizable with its set of lattice fringes at 3.12 Å (111), 2.71 Å (200), and 1.91 Å (220) for the cubic phase. It is covered with many smaller crystallites of various cobalt compounds, among which we did not identify pure cobalt but rather often CoO or Co_3O_4 particles. Figure 13 shows a very clear example of this type and in Fig. 14 we see a detail in which a CoO particle is directly attached on top of a CeO_2 crystal. It has to be added that this specimen is rather sensitive to beam damage, noticeable changes occurring over time periods of a few minutes. Another point worth mentioning is the clear white halo fringing the RE oxide crystal in many cases. As its intensity is higher than the vacuum level, it has to be attributed to a focusing effect in this area for which the most likely interpretation is the presence of an electric field induced by a

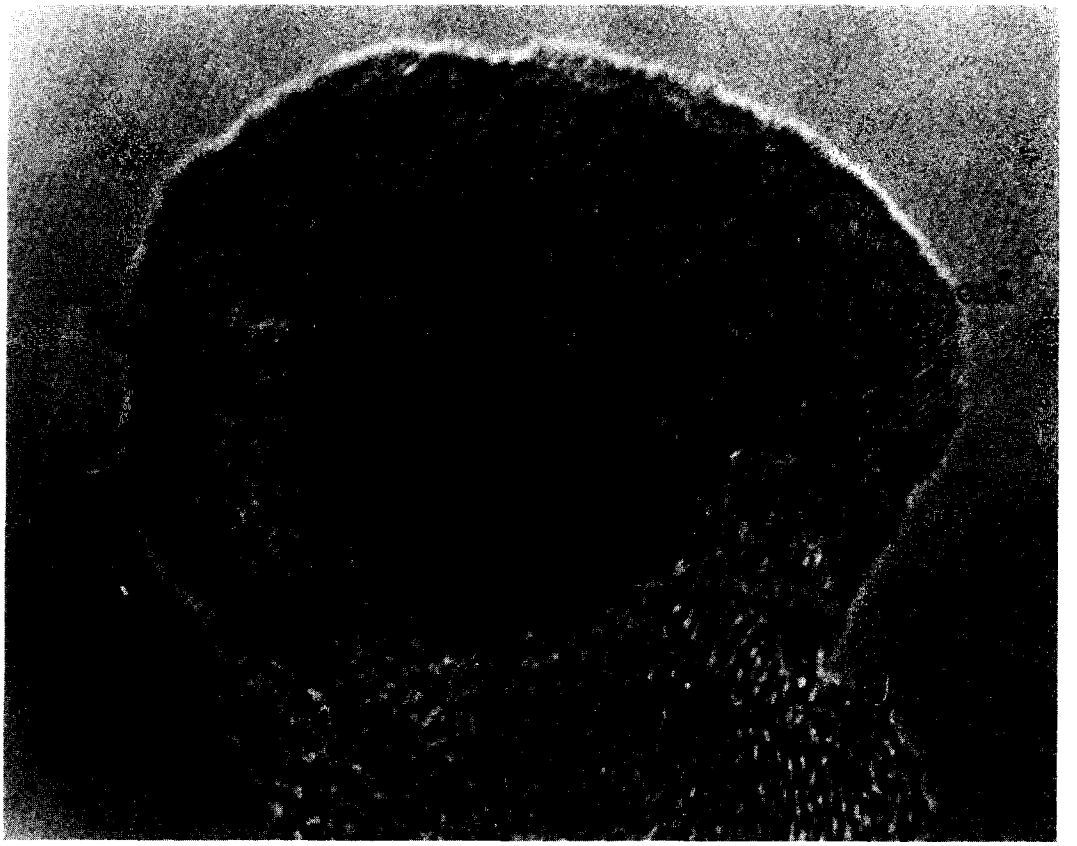

FIG. 11. In specimen Co/La_2O_3 one finds Co particles at the extremity of carbon fibers; they are, however, partially covered with CoO crystallites, similarly to the $LaCo_5$ specimen.

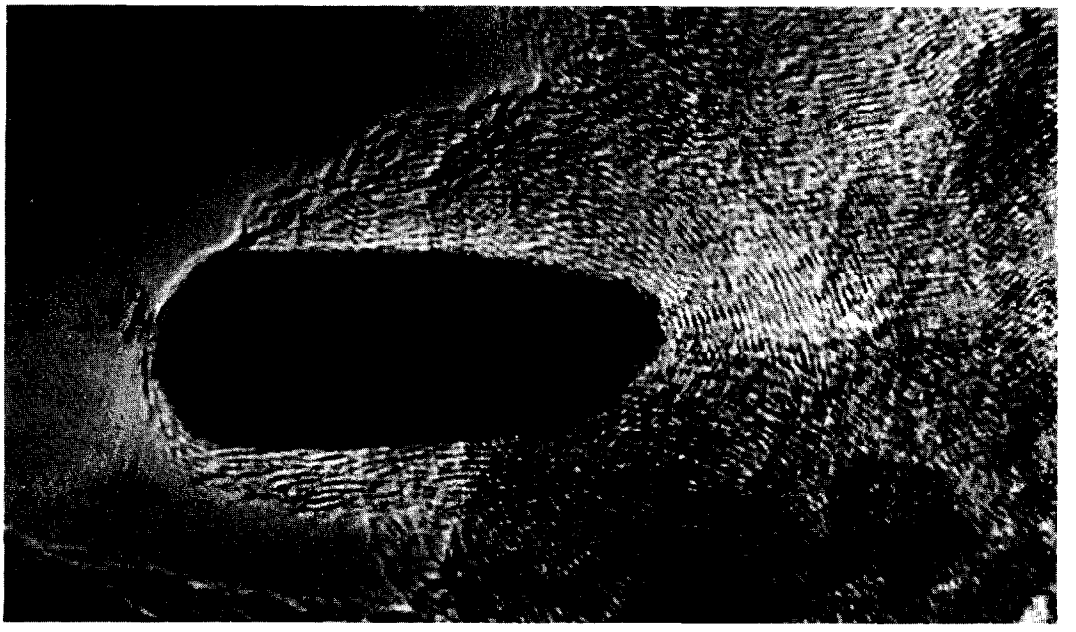

FIG. 12. An isolated faulted Co particle in specimen Co/La_2O_3.

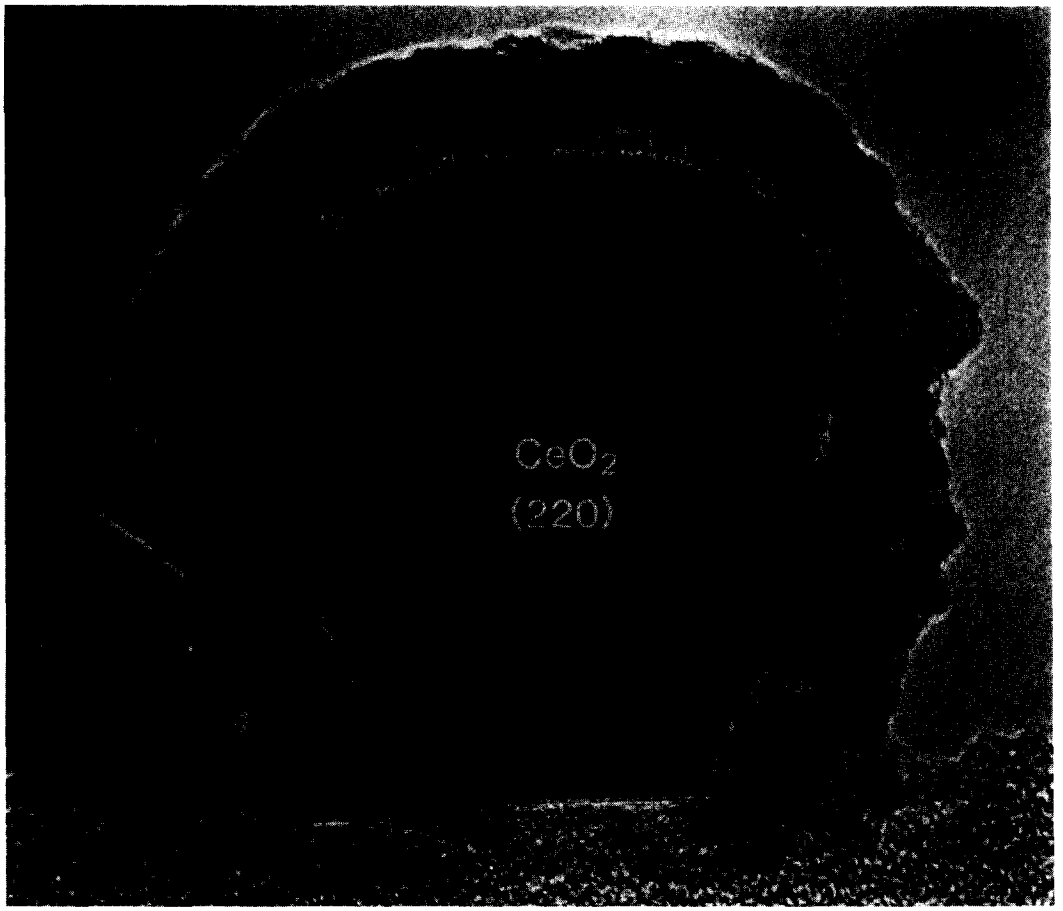

FIG. 13. An example of the general arrangement in specimen Co/CeO_2. The well-defined RE oxide crystal in the middle is covered with an irregular deposit of Co compounds, a few of them being the easily identifiable CoO and Co_3O_4 ones, but not of all being recognizable. This specimen is highly beam sensitive. Note the strong white contour around the RE oxide particle. It is likely due to focusing of the beam along the electrically charged surfaces of this strong insulator.

strong charging effect on the surface of this insulator. This behavior is more important for this specimen due to the lack of the thin catalytic carbon coating which helps eliminate the charges induced by the primary beam.

5. *General Remarks about Specimen Changes under the Beam*

Intense incident electron doses may induce modifications, i.e., permanent alterations in chemistry and structure, by radiation damage. Some evidence of such changes has been obtained while continuously tape recording HREM images with the high-voltage EM operated at 300 kV.

Figure 15 shows two successive micrographs of the same area, with an irradiation dose difference of about 10^8 e^-/nm^2 between them (this corresponds to a current density of 5 A/cm^2 on the specimen and 10 min irradiation time). While the regular lattice fringe system is preserved on the cobalt particle, one notices clear changes outside of it and on the free surface. It means that there is no clear transformation or amorphization of the bulk of the metal, the most sensitive areas being interfaces and sur-

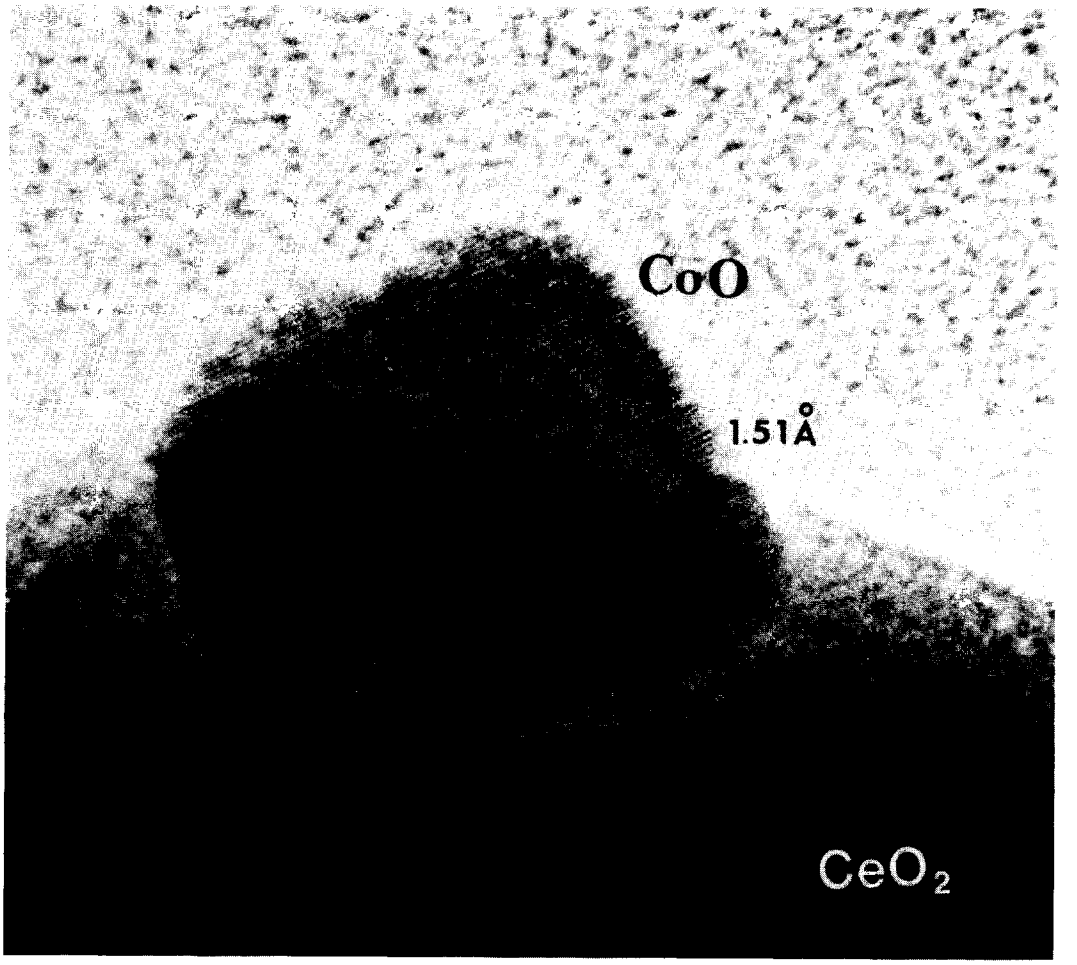

FIG. 14. A small CoO crystallite in specimen Co/CeO_2 attached on the surface of a CeO_2 crystal.

faces (and maybe all other types of defects). For instance small crystallites of one to a few nanometers in size appear or disappear on the surface (circled areas 1 to 4). There is also a clear transfer of cobalt atoms from the main cobalt particle toward the surface with the nucleation of a new unidentified product (shrinkage of area 6 and enlargement of area 5). The thickness of the catalytic carbon layer has also been modified.

All these processes are rather complex and at the present time only qualitative arguments can be proposed. This is a three-component interaction involving the specimen (with cobalt, oxygen, carbon), the microscope column vacuum (with a non-negligible partial pressure in oxygen), and the primary electron beam continuously depositing energy into this "submicroscope reaction chamber." At 300 kV, the energy transferred in knock-on collisions is sufficient to displace light atoms such as carbon and oxygen, but not cobalt (see for instance Hobbs (*21*)). More probable is an enhanced defect or atom diffusion under the beam. The energy necessary to propagate an existing interstitial is much less than that required to create a Frenkel pair. Moreover the direct momentum transfer is responsible for a number of defects much larger than the average one at thermal equilibrium. Similar changes have also been detected for reduced primary voltages (200

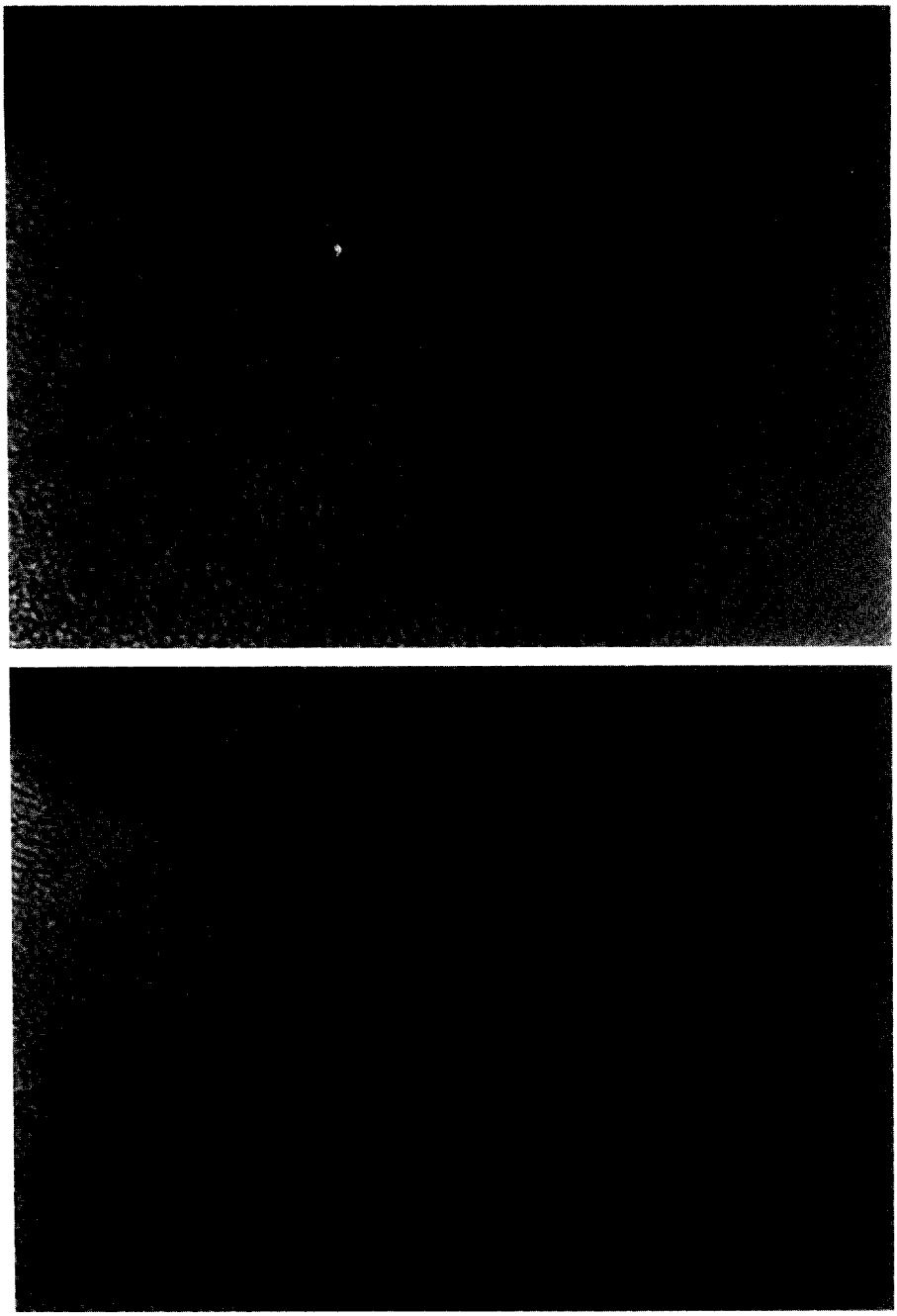

FIG. 15. Two successive micrographs at 300 kV with 10 nm of irradiation between them. See text for discussion of the detectable specimen modifications induced by the primary electron beam.

kV), more particularly on the Co/CeO_2 specimens, as a consequence of already mentioned charging effects. Figure 16 illustrates this effect: one sees a series of modifications within the object, such as the shrinkage of the RE oxide crystal which also seems to rotate on itself, while many modifications can be detected among the different smaller particles which cover it. All these features have strong similarities

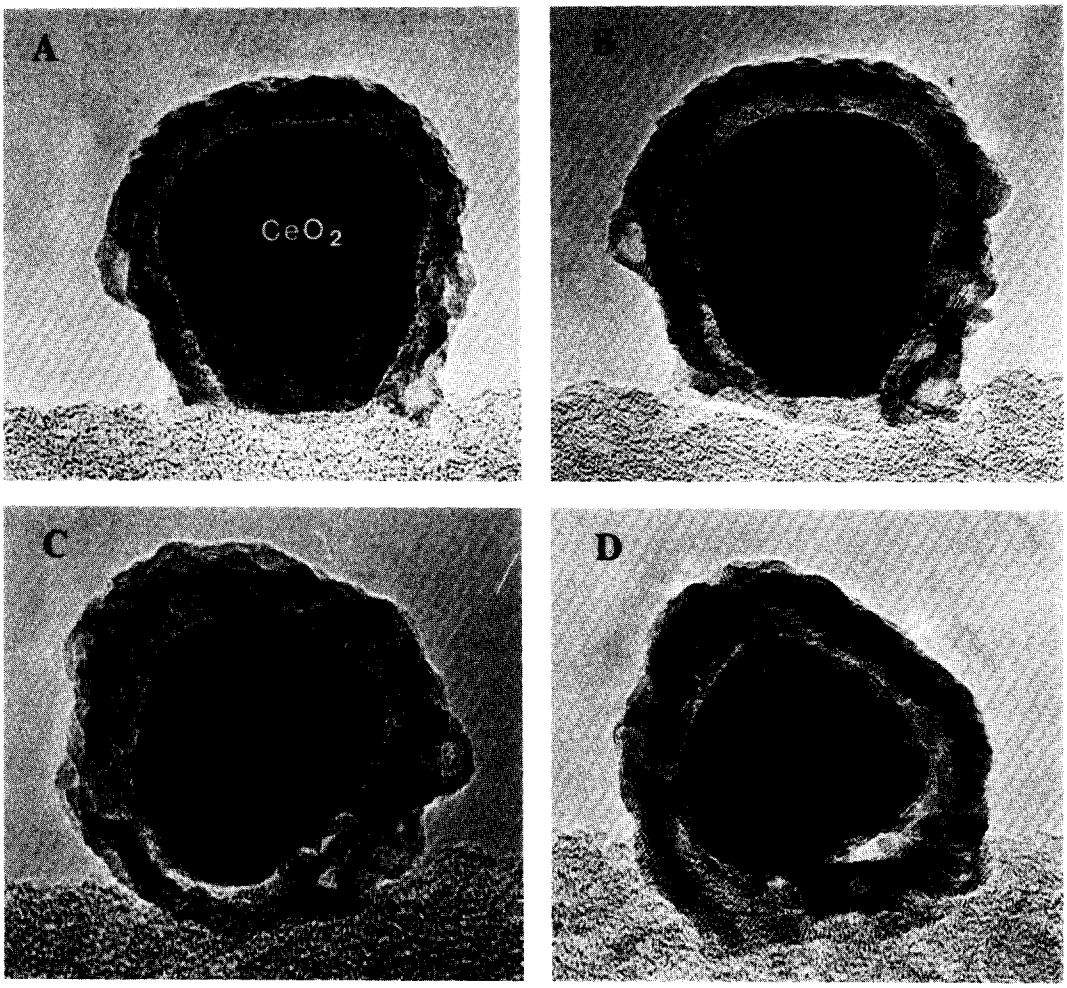

FIG. 16. A series of micrographs separated by intervals of ≃3 min illustrating the changes of specimen Co/CeO_2 under the beam.

with beam-induced movements of small metallic clusters already described in the literature (*22*), or with beam-induced reduction or oxidation processes which meant that the electron microscope behaves as a high-performance chemical reactor for the preparation of phases out of the thermal equilibrium (*23*). As a consequence, we have found that it is not always possible to identify the particles present on the surface of the rare earth oxide, and in a few cases we have hints of the production of some compounds between the metal cobalt and the rare earth. It seems possible to index a few optical diffraction patterns of lattice images as due to $LaCo_2$. It would constitute a beam-induced alloying transformation, to some extent a reverse of the catalytic (CO, H_2) one, which disrupts a cobalt–RE alloy into a metal oxide support system. This is not very surprising because a major effect of these moderately high voltages is to sputter the low Z elements from the specimen, in the present case the carbon and oxygen atoms.

However, all these exotic phases are of little relevance for understanding the behavior of the intermetallic or metal–support catalysts in the syngas reaction. The important question is, "Are all the phases ob-

served in the specimen real products of the catalytic reaction or are they artifacts induced a posteriori and more particularly during the observation under the electron beam?" At the present stage of investigation, observations at lower voltages (100–120 kV) and in better vacuum environment seem stable even if they require more intense doses. Consequently, the detection of oxygen and the identification of cobalt oxides seem real results and not artifacts induced by the electron microscope. These results also confirm some of the EXAFS results mentioned in the introduction.

DISCUSSION OF THE RESULTS AS COMPARED WITH THE CATALYTIC PROPERTIES

The above observations concerning the $LaCo_5$ (a) and (d) compounds, as well as the Co/La_2O_3 one, agree satisfactorily with the EXAFS and XANES data on the CoK edge (*3*). Although the catalytic precursors are different for these two types of catalysts, the cobalt environment is nearly the same at the completion of the catalytic reaction:

(i) cobalt particles are partially oxidized into the CoO and Co_3O_4 species identified by HREM on the free surface of the metal;
(ii) cobalt particles are isolated from the lanthanum oxide by the layer of active carbon deposited during the reaction.

This likeness of cobalt environment explains the similarities between the catalytic properties. This was rather unexpected because for $LaNi_5$ and Ni/La_2O_3 very distinct catalytic properties had been observed (*24*). Considering the cobalt–lanthanum catalysts, CH_4 is the major product of the reaction, with CO_2 being a secondary product of equivalent importance (see Table 1), which can be deduced from the following chemical reaction:

$$2CO + 2H_2 \rightarrow CH_4 + CO_2$$

which comes from

$$2xCO + Co \rightarrow CoC_x + xCO_2$$

$$CoC_x + 2H_2 \rightarrow CH_4 + CoC_{x-1}.$$

However, this selectivity range is very different from the case of carbon-supported cobalt catalysts (*25*), in which case mostly CH_4 is produced while oxygen is evacuated as water. This comparison proves that the rare earth oxide is involved in the activation process although it is isolated from the cobalt by the carbon layer.

The Co/CeO_2 case is completely different when considering the cobalt environment:

(i) Cobalt particles are not covered by catalytic carbon layers but are directly supported on CeO_2.
(ii) Cobalt particles are strongly oxidized.

EXAFS and XANES studies had already given some evidence of a cobalt environment very different from the Co–La system. It did not only show a partially fcc cobalt, but it could not even provide the exact cobalt environment. As indicated, again in Table I, the catalytic properties themselves are quite different:

(i) The catalyst is rather inactive.
(ii) Only CO_2 is produced.

In this case, similar catalytic characteristics have been observed for the Ni/CeO_2 system reduced at the same temperature of 400°C (*24*). It has been attributed to a strong metal–support interaction (SMSI) observed for other systems such as Pd/La_2O_3 or TM/TiO_2 (*26–28*). The recently observed variation in adsorption and catalytic properties could be attributed to the transfer of CoO_x species to the surface of the metal particles during the catalytical activation. New reaction sites could then be created allowing CO but not H_2 adsorption. Nevertheless it is difficult to provide an evidence of CeO_x transfer on the Co particles. The only salient feature is the close contact between Co and CeO_2. As CeO_2 is an insulator and retains the electronic charges as illustrated in the micrographs, it could be responsible for a change of the electronic properties of the deposited Co particles, and consequently modify the metal catalytic properties.

In order to explain the difference of behavior between lanthanum and cerium for carbon accommodation, one can refer to some results obtained by Dexpert *et al.* (*29*). The authors had observed a difference in carbon deposition under the electron beam over surfaces of Nd_2O_3 and Y_2O_3 microcrystals. They explained it by invoking a more appropriate fitting of the catalytic carbon interreticular distances with the (111) plane of the cubic Y_2O_3. In the present case, CeO_2 is cubic with a 3.12-Å plane distance in the (111) direction, while the hexagonal structure La_2O_3 has a 3.42-Å lattice plane spacing in the $(10\bar{1}0)$ direction. When considering the matching of the lattice plane distances to the catalytic carbon lattice fringes which vary from 3.4 to 3.5 Å, La_2O_3 crystals are more likely covered by catalytic carbon.

CONCLUSIONS

Using several high-resolution electron microscopy techniques, this work has provided a rather detailed description of the catalytic site for $LaCo_5$, Co/La_2O_3, and Co/CeO_2 compounds. The dispersive role of the carbon is clearly observed for $LaCo_5$ and Co/La_2O_3. It grows from the cobalt particle and is attached on the lanthanum platelets, producing a cobalt, carbon, lanthanum oxide complex system. The similarity of the cobalt environment in both systems explains the similarity of their catalytic properties.

In the case of Co/CeO_2, the catalytic site is completely different; the cobalt particles are strongly oxidized and lie on CeO_2 without a carbon layer. As the catalytic properties are very similar to those of Ni/CeO_2 and other systems where SMSI has been observed, we can reasonably propose a similar behavior for Co/CeO_2. The close contact of Co with CeO_2 could induce electronic changes in the transition metal properties and induce such unusual catalytic properties.

ACKNOWLEDGMENTS

This work was supported by the U.S. Department of Energy under Contract DE-FG02-86 ER 45228 and has made use of the resources of the ASU Facility for HREM, supported by NSF Grant DMR 83 06501. One of us (C.C.) thanks the Department of Physics and the Center for Solid State Science for their support and hospitality during his stay at ASU. We would like to thank J. M. Cowley for his permanent interest and useful comments and J. Barry for his skillful assistance during the 4000EX work.

REFERENCES

1. Barrault, J., Duprez, D., Guilleminot, A., Percheron-Guegan, A., and Achard, J. C., *Appl. Catal.* **5,** 99 (1983).
2. Chin, R. L., Elattar, E., Wallace, W. E., and Hercules, D. M., *J. Phys. Chem.* **84,** 2895 (1980).
3. Barrault, J., Guilleminot, A., Achard, J. C., Paul-Boncour, V., Percheron-Guegan, A., Hilaire, L., and Coulon, M., *Appl. Catal.* **22,** 273 (1986).
4. Audier, M., Oberlin, A., Oberlin, M., Coulon, M., and Bonnetain, L., *Carbon* **19,** 217 (1981).
5. Watson, P. R., and Castner, D. G., *in* "3rd International EXAFS Conference," Stanford (1984).
6. Paul-Boncour, V., personal communication (1985).
7. Lagarde, P., Murata, T., Vlaic, G., Freund, E., Dexpert, H., and Bournonville, J. P., *J. Catal.* **84,** 333 (1983).
8. Audier, M., and Guyot, P., *J. Microsc. Spectrosc. Electron.* **8,** 261 (1983).
9. Audier, M., and Guyot, P., *J. Microsc. Spectrosc. Electron.* **10,** 8 and 17 (1985).
10. Wang, Z. L., Colliex, C., Paul-Boncour, V., and Percheron-Guegan, A., *in* "Proceedings, 44th EMSA," p. 768. San Francisco Press, San Francisco, 1986.
11. Cliff, G., and Lorimer, G. W., *J. Microsc.* **103,** 203 (1975).
12. Zaluzec, N., *in* "Introduction to Analytical Electron Microscopy" (D. Joy, J. Hren, and J. Goldstein, Eds.), p. 121. Plenum, New York, 1979.
13. Colliex, C., *in* "Advances in Optical and Electron Microscopy", (R. Barer and V. Cosslett, Eds.), Vol. 9, p. 65. Academic Press, Orlando, FL, 1984.
14. Wehenkel, C., and Gauthé, B., *Phys. Status Solidi (b)* **64,** 515 (1974).
15. Ahn, C. C., and Krivanek, O. L., "An Atlas of EELS Spectra." Available from the Secretary, Center for Solid State Science, ASU Tempe, AZ 85287 (1982).
16. Egerton, R. F., *Ultramicroscopy* **3,** 243 (1978).
17. Egerton, R. F., *Ultramicroscopy* **4,** 169 (1979); Egerton, R. F., *Scanning Electron Microscopy,* 505 (1984).

18. Smith, D. J., Fisher, R. M., and Freeman, L. A., *J. Catal.* **72,** 51 (1981).

19. Cowley, J. M., *in* "Diffraction Physics," 2nd ed., Chap. 18, p. 289. North-Holland, Amsterdam, 1981.

20. Bernal, S., Diaz, J. A., Garcia, R., and Rodriguez-Izquierdo, J. M., *J. Mater. Sci.* **20,** 537 (1985).

21. Hobbs, L. W., *in* "Introduction to Analytical Electron Microscopy" (J. Hren, J. Goldstein, and D. Joy, Eds.), p. 437. Plenum, New York, 1979. Hobbs, L. W., *in* "Quantitative Electron Microscopy" (J. Chapman and A. Craven, Eds.), Vol. 25, p. 399, Scottish Universities Summer School in Physics, 1984.

22. Wallenberg, L. R., Bovin, J. O., and Schmid, G., *Surf. Sci.* **156,** 256 (1985).

23. Eyring, L., Dufner, C., Goral, J. P., and Holloway, A., *Ultramicroscopy* **18,** 253 (1985).

24. Guilleminot, A., thesis, Poitiers, France, 1984.

25. Barrault, J., Guilleminot, A., Achard, J. C., Paul-Boncour, V., and Percheron-Guegan, A., *Appl. Catal.* **21,** 307 (1986).

26. Hicks, R. F., Yen, Q. J., and Bell, A. T., *J. Catal.* **87,** 398 (1984).

27. Mitchell, M. D., and Vannice, M. A., *Ind. Eng. Chem. Fundam.* **23,** 88 (1984).

28. Anderson, J. B. F., Bracey J. D., Burch, R., and Flambard, A. R., *in* "Proceedings, 8th International Congress on Catalysis, Berlin," 1984, Vol. 5, p. 111.

29. Dexpert, H., Pennycook, S. J., and Brown, L. M., *Inst. Phys. Conf. Ser.* **52,** 339 (1980); Dexpert, H., private communication (1986).